

Mechanistic insights into temperature hysteresis in CO oxidation on Cu-TiO₂ mesosphere

Wen-Ta Yang ^{a,b,c}, Li Cheng Kao ^{d,*}, Xian-Teng Yu ^e, Chung-Li Dong ^f, Sofia Ya Hsuan Liou ^{a,b,c, **}

^a Department of Geosciences, National Taiwan University, Taipei 106, Taiwan

^b Research Center for Future Earth, National Taiwan University, Taipei 106, Taiwan

^c Science and Technology Research Institute for DE-Carbonization (STRIDE-C), NTU, Taipei 106, Taiwan

^d Department of Resources Engineering, National Cheng Kung University, Tainan 701, Taiwan

^e Department of Mechanical, Engineering National Taipei University of Technology, Taipei 106, Taiwan

^f Research Center for X-ray Science & Department of Physics, Tamkang University, New Taipei City 25137, Taiwan



ARTICLE INFO

Keywords:

In-situ XAS
Operando Raman
CO oxidation
Copper/titanium dioxide
Oxygen replenishment

ABSTRACT

This study employs in-situ X-ray absorption spectroscopy (XAS) and operando Raman to explore the reaction mechanism of copper/titanium dioxide microspheres (CuTMS) in CO oxidation. A temperature-dependent hysteresis behavior was observed during catalytic CO oxidation, which can be divided into two distinct regions. In the low-temperature region, the transformation of CuO → Cu₂O → Cu₂O/Cu on the surface of CuTMS is detected via in-situ XAS, highlighting the pivotal role of surface-adsorbed oxygen in initiating this conversion process. Conversely, in the high-temperature region, analysis of Raman peak areas suggests a variation in the {001} and {101} facets of anatase. Specifically, a decrease in the {001} facets from 17% to 10% indicates TiO₂-mediated oxygen transportation, which facilitates the reoxidation of reduced Cu species. This integrated approach showcases significant potential for unraveling the mechanistic studies of catalytic reaction mechanisms in copper/titanium systems, including surface copper valence state changes, oxygen replenishment, and crystal structure distortion.

1. Introduction

In light of the contemporary focus on advancing green energy technologies, comprehending the catalytic carbon monoxide (CO) oxidation mechanism has regained prominence in recent years. This resurgence stems from the realization that during the green energy production processes of third-generation biofuels and green hydrogen, CO can inadvertently emerge as a harmful by-product [1]. The CO as resources of main/by products in several hydrogen production process to produce hydrogen, such as: oxidation steam reforming (OSR) [2–4], water-gas shift reaction (WGSR) [5], preferential oxidation (PROX) [6] and photoreforming [7]. The potential release of substantial quantities of CO into our environment not only jeopardizes the sustainability of production processes but also undermines energy efficiency. Consequently, investigating the mechanism of the catalytic CO oxidation reaction has emerged as a critical research endeavor. Such efforts are essential for devising pathways for green energy production and improving product

selectivity. The study of CO reformation is important for addressing the challenges of sustainable energy production and reducing the environmental impact of industrial processes [8]. Building upon Haruta et al.'s groundbreaking research in 1987 [9], extensive studies have delved into noble metal doping to enhance the catalytic performance of materials for CO oxidation, facilitating operation at ultralow-temperatures. However, in the early 2000s, attention gradually shifted toward the development of non-noble metal-based materials and catalysts capable of sustained performance above room temperature, for industrial catalytic applications and commercial viability [10–13].

While the reaction mechanism of catalytic CO oxidation remains subject to debate, research on noble metals for CO oxidation has spanned decades [14,15]. The reaction mechanisms of catalytic CO oxidation can be broadly classified into four categories: (1) surface reactions occurring directly on the doping metal [16–19]; (2) CO oxidation occurring at interfacial sites, such as step edges [20–24]; (3) involvement of surface oxygen vacancies within the material to facilitate the

* Corresponding author.

** Corresponding author at: Department of Geosciences, National Taiwan University, Taipei 106, Taiwan.

E-mail addresses: lckao@gs.ncku.edu.tw (L.C. Kao), yhliou@ntu.edu.tw (S.Y.H. Liou).

reaction [25–27]; and (4) donation of oxygen from the lattice oxygen of the supporting metal oxide (MO_x) [28–31]. Recent studies have suggested that the Mars-van Krevelen (M-v-K) type reaction emerges as the predominant reaction mechanism in doped metal-oxide catalyst systems [20,26,29,30]. These findings underscore the importance of further explorations into heterogeneous catalysis, particularly focusing on the correlation between the active doping metal and the supporting MO_x [32]. Doping of copper-based materials into supported MO_x facilitates catalytic CO oxidation by leveraging a synergistic effect. In our previous research, we demonstrated that copper/titanium dioxide materials exhibit an active site within the Cu-O-Ti structure, with the catalytic CO oxidation performance notably influenced by temperature [33]. Doped metal oxide catalysts equipped with a Metal-Oxide-Metal' (M-O-M') structure have demonstrated efficacy in catalytic oxidation because of the contribution of surface lattice oxygen and the formation of oxygen vacancies [34]. Raman spectroscopy has emerged as a widely used structure-sensitive technique for characterizing material vibration modes, offering superior capability in identifying anatase and rutile phases compared with X-ray diffraction (XRD) [35]. Furthermore, recent studies have highlighted the utility of Raman spectroscopy in estimating material crystal facets, presenting a novel approach for material characterization [36]. In addition, Raman spectroscopy is increasingly recognized as an effective method for monitoring oxygen vacancies in advanced applications. Its resilience to atmospheric conditions, coupled with a precise laser light source, renders it widely customizable to different reaction conditions.

Building upon these advantages, Bañares et al. pioneered the concept of “operando,” an analytical methodology for real-time monitoring of the structure-reaction relationship under actual reaction conditions [37]. Sécordel et al. used operando Raman spectroscopy to demonstrate how the M-O-M' structure was impacted by oxygen introduction during the reaction [38]. In 2020, significant insights into the correlation between catalyst structure and hysteresis behavior during CO oxidation were uncovered using in-situ Bragg coherent X-ray techniques. Subsequently, in 2021, further evidence emerged indicating that defect formation was dependent on the reaction temperature [39,40]. These promising findings underscore the potential of integrating various characterization techniques to adopt a multifaceted approach toward unraveling the reaction mechanism and the intrinsic properties of the active catalyst phases.

In this study, we developed a CO temperature-programmed reduction (CO-TPR) tandem oxygen temperature-programmed oxidation (O_2 -TPO) analysis sequence to validate the oxygen resupply behavior [41]. In addition, we employed operando Raman spectroscopy to uncover crystal structure distortions and in-situ X-ray absorption spectroscopy (XAS) to elucidate variations in the electronic configuration of surface species. The objective of this research was to devise a comprehensive approach aimed at unveiling the reaction mechanism for catalytic CO oxidation by a copper/titanium dioxide system during hysteresis.

2. Experiments and methods

For comparison, the material employed in this study was synthesized using the same method as that used in our previous research, namely the one-step aerosol-assisted self-assembly (one-step AASA) technique [33]. In our earlier work, we found that the material CO oxidation ability followed the order of the Cu:Ti ion percentage ratio: 20:100 > 25:100 \approx 10:100 > 3:100 > 0:100. Notably, Cu:Ti = 20:100 exhibited optimum copper-loading condition; therefore, the sample with an overload ratio of 25:100 was not considered for the CO oxidation catalyst. Moreover, while the 3:100 ratio proved less effective, we employed Cu:Ti catalyst ratios of 1:100 and 5:100 in this study to gain further insights into the rule for copper loading in the copper/titanium catalyst system. The copper titanium mesosphere is labeled as Cu_xTMS , where X is the Cu:Ti percentage ratio of the ICP result.

2.1. Catalyst characterization

The chemical compositions of the materials were analyzed using inductively coupled plasma-optical emission spectroscopy/mass spectrometry (ICP-OES/MS) (Thermo iCAP 7000). The sample was microwave-digested using CEM MARS 6 by CEM Corporation, USA. For digestion, 0.1 g of Cu/TiO₂ microspheres (CuTMS) was combined with a mixture of HCl and HNO₃ at a ratio of 1:3 in 50-ml polypropylene tubes. The digestion process involved heating the tubes at 120°C for 10 min, followed by a holding period at 180°C for 10 min (ramp = 10 °C/min, 100 W for each vessel). The digested samples were then filtered using a 0.45-μm membrane and quantified. Material thermogravimetric analysis (TGA) and differential thermogravimetric analysis (DTG) were conducted using a SDT Q600 by TA Instruments with a sample size of ~10 mg. Nitrogen gas was used as the purge gas and maintained at a constant flow rate of 100 ml/min. The experiments were carried out in a temperature range of 50°C–500°C, with a heating rate of 10 °C/min. Copper dispersion was observed using a high-resolution scanning transmission electron microscope equipped with a high-angle annular dark field detector (HR STEM-HAADF, FEI by Thermo Fisher Scientific) and Talos F200XG2 operated at 200 kV, equipped with a Super-X energy-dispersive X-ray spectroscopy (EDS) system comprising four silicon drift detectors. Crystal characterization of CuTMS was performed using a DXR3 Raman microscope by Thermo Scientific, with a laser line at 532 nm and a He-Cd laser as the excitation source with a maximum output power of 10 mW. The power of the laser on the CuTMS samples was 0.1 mW. Spectra were collected twice for 0.5 s each, with a spectral resolution of 2 cm⁻¹.

2.2. Catalytic CO oxidation and chemical adsorption analysis

Before conducting the chemical/catalytic measurements, without specification, the as-prepared CuTMS material underwent pretreatment. Initially, it was exposed to 4% oxygen in argon (60 ml/min), heated from room temperature to 350°C, and maintained at this temperature for 30 min with a ramp of 10 °C/min. Subsequently, the material was purged with argon for 1 h to eliminate residual gases during the cooling process. The reaction conditions were controlled within 1%CO:1% O_2 :98%Ar (60 ml/min) using a mass flow controller (Brooks 0254) equipped with a flow meter (Brooks 5850E). The CuTMS catalytic CO oxidation were carried under 100,000 gas hourly space velocity (GHSV). The reaction was conducted within a custom-built module featuring a portable mass flow controller integrated with the furnace reaction system, as illustrated in Fig. S1. The CO oxidation ramping is controlled at 2 °C/min for better monitoring of the catalytic procedure.

To investigate the self-reduction ability of CuTMS by CO and the further oxygen replenishment phenomenon, a CO-TPR was conducted concurrently with an O_2 -TPO. The gas output was detected in real-time using a mass spectrometer (Hiden HPR-20 R&D). In addition, to provide more detailed insights, the reactions of CO, O_2 , and relative formation of CO_2 (m/z = 28, 32, and 44 respectively) were also recorded. Approximately 100 mg of freshly prepared CuTMS was weighed and loaded into a silica bed quartz tube. The reaction atmosphere was maintained at 15 ml/min comprising 4% CO balanced with Ar, to achieve the CO-TPR result. Subsequently, without exposure to air, O_2 -TPO was performed using 4% O_2 balanced with Ar at 15 ml/min. The sequence of chemisorption measurements involved heating to 800°C, with ramping at 10°C/min, to reveal the effect of the copper sites on CO oxidation. For more detailed information on the experimental conditions where is organized and presented in supporting information in Table S.1.

2.3. Synchrotron-based XAS

The ex-situ Cu K-edge XAS spectra were collected in fluorescence mode and were recorded at beamline 12B2 in Spring-8 of the Taiwan beamline of the National Synchrotron Radiation Research Center

(NSRRC). The electron storage ring was operated at 8.0 GeV with a constant current of \sim 100 mA. The incident beam energy was monochromatized using a Si (111) double crystal monochromator. XAS data were measured from 150 eV below to 800 eV above the absorption edge and thereby cover the X-ray absorption near edge structure (XANES) and extended X-ray absorption fine structure (EXAFS) regions. Data were deglitched by manually removing single sharp outlier points before merging identical datasets in Athena. The program Athena was used to perform data corrections and analysis including background subtraction, data normalization, extraction of the EXAFS signal, Fourier transformation (FT), and data refinement in R-space. In-situ XAS at O K-edges were obtained at TLS (Taiwan Light Sources) BL20A, NSRRC with a resolving power of approximately 8000. The in-situ XAS at the Cu and Ti K-edge was obtained at TLS BL17C. A double-crystal Si (111) monochromator was used for energy selection, with an energy resolution ($E/\Delta E$) of about 7000. In-situ XAS was carried out with a homemade in-situ gas flow cell to determine its atomic/electronic structure in its operating mode.

2.4. Operando technique for reaction observation

To observe the reactions at varying temperatures, a dynamic gas flow cell-equipped with an operando Raman tandem real-time mass spectrometer was used. The Raman microscope was positioned atop a heating stage (Linkam Scientific-TS1500) with a temperature control capability of 0.2 s/point, facilitating the observation of the CO oxidation process and intermediate material crystalline changes. The reaction gas was also controlled by Brooks; the ramp and other conditions were set identical to those of the CO oxidation reaction process. The exhaust gas was introduced into the real-time mass spectrometer, the buildup operando Raman tandem real-time mass system, as shown in Fig. 1. Operando Raman spectra were collected twice for 20 s each, spanning from room temperature to 250°C. The entire spectral range of 100–3500 cm⁻¹ was covered during data acquisition. Operando Raman peak details were obtained using Thermo OMNIC TQ Analyst software for identification.

3. Results and discussion

3.1. CuTMS CO oxidation hysteresis behavior and the role of copper

Copper plays an indispensable role in the Cu/TiO₂ system for catalytic CO oxidation. To perform an intensive study of the copper effect in copper-doped titanium system catalysts, we conducted chemical

analysis of CuTMS and obtained the weight percentage results of copper-loading using ICP-OES/MS. The results are listed in Table 1. The remaining catalyst components consisted of Ti and O atoms. Hereinafter, the obtained copper weight percentage is labeled as x, and the synthesized mesoporous Cu-doped TiO₂ microspheres are referred to as Cu_xTMS.

The catalytic CO oxidation behaviors of TMS, Cu_{2.1}TMS, Cu_{4.2}TMS, and Cu_{8.5}TMS were evaluated as shown in Fig. 2(a). For brevity, the CO oxidation mass spectra of the Cu_{0.4}TMS and Cu_{1.2}TMS materials, along with further material characteristic analyses, are included in the supplementary information (Fig. S2). It was observed that the CO oxidation ability of Cu_xTMS improved with increasing copper loading. The complete CO conversion temperature decreased, indicating that Cu_xTMS catalytic CO oxidation could be performed at lower temperatures. Interestingly, CuTMS materials exhibited a hysteresis phenomenon, which is a typical behavior in heterogeneous doped metal-oxide catalyst CO oxidation. Typically, this phenomenon is considered an ignition/extinction process [42,43]. However, in this study, it was observed as a clue to trace the influence of changes in the material lattice oxygen. The three-cycle reuse performance result of Cu_{8.5}TMS is presented in Fig. 2(b) to prove that the as-synthesized Cu_{8.5}TMS catalyst did not pollute or destroy the structure during the ignition/extinction process. The duplicate test results for Cu_{8.5}TMS revealed a similar CO oxidation hysteresis behavior, indicating not only high reusability but also material structure stability across different batch reactions.

The HAADF-STEM-EDS mapping images are illustrated in Figs. 3(a) and 3(b) reveal the distinction between the newly employed Cu_{2.1}TMS and the best-performing Cu_{8.5}TMS. Compared with the HAADF-STEM-

Table 1
Chemical analysis by ICP-OES/MS for CuTMS.

Sample name	Cu:Ti ratio ^a	Sample weight ^b (mg)	Copper concentration ^c (ppm)	Copper weight percentage ^d (%)
TMS	0:100	109.50	-	-
Cu _{0.4} TMS	1:100	114.40	8.96	0.44
Cu _{1.2} TMS	3:100	116.50	24.22	1.21
Cu _{2.1} TMS	5:100	113.10	41.67	2.08
Cu _{4.2} TMS	10:100	110.00	84.11	4.21
Cu _{8.5} TMS	20:100	110.60	170.07	8.50

^a The idea copper loading in mole ratio

^b The original sample weight for microwave digestion

^c Copper concentration in 50 ml dilute solvent

^d Copper weight percentage in CuTMS sample

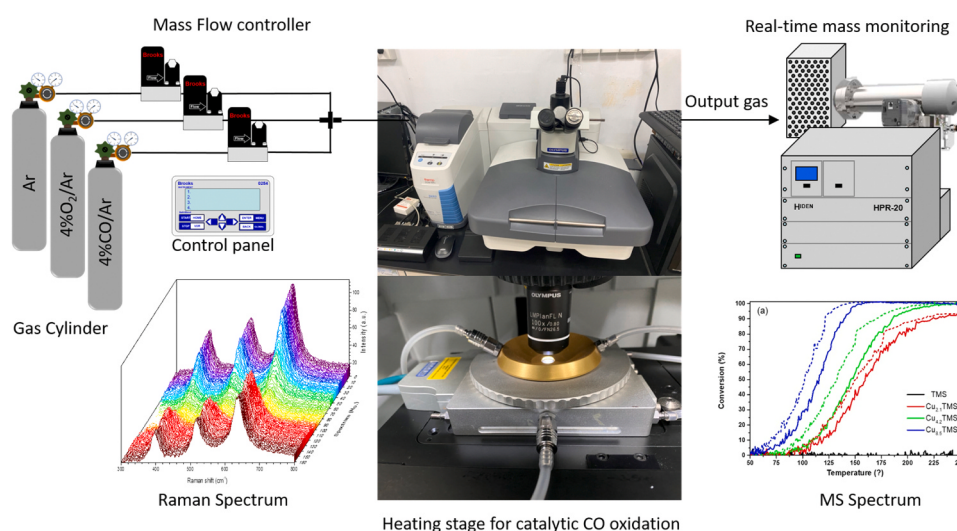


Fig. 1. Scheme of the plausible system of operando Raman tandem real-time mass.

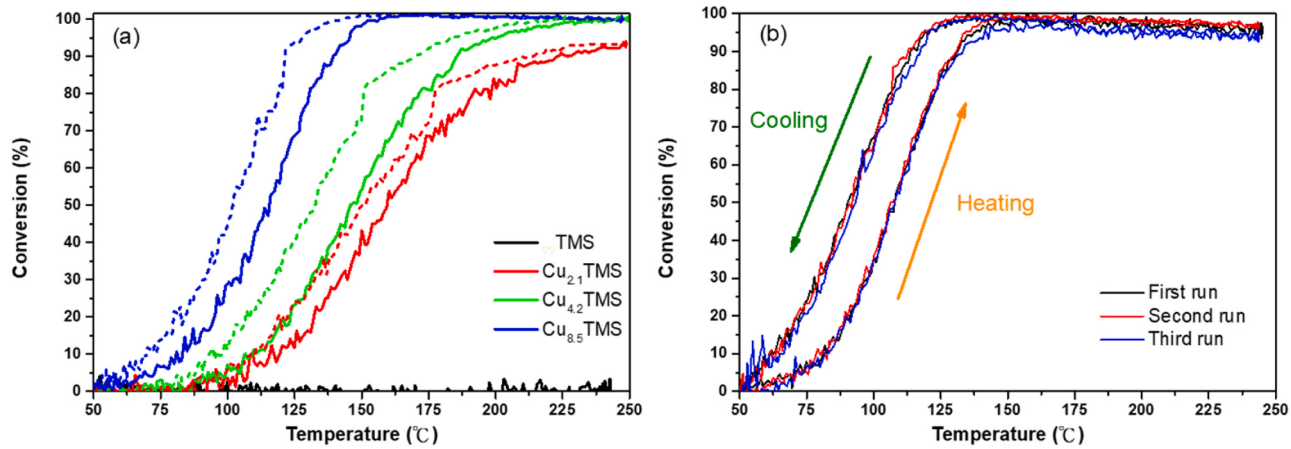


Fig. 2. (a) Catalytic activity during CO oxidation heating (solid lines) and cooling (dash lines) over materials with different copper contents. (b) Results of a three-cycle CO oxidation temperature-looping experiment on Cu_{8.5}TMS (The experiment ramping is indicated by arrows, CuTMS 1%CO:1%O₂:98%Ar =60 ml/min, ramp= 2 °C/min.).

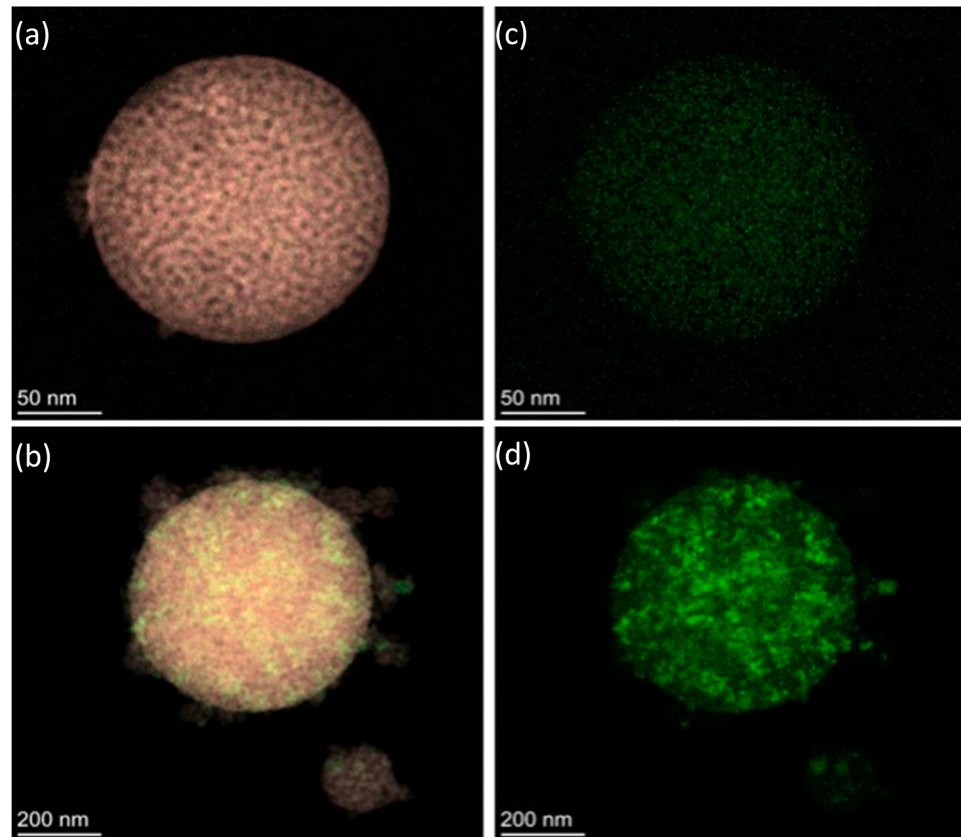


Fig. 3. HAADF-STEM-EDS mapping image of (a) Cu_{2.1}TMS and (b) Cu_{8.5}TMS overlap with red, Ti-L and green, Cu-K, EDS mapping of copper of (c) Cu_{2.1}TMS and (d) Cu_{8.5}TMS.

EDS mapping result of copper in Figs. 3(c) and 3(d) (with oxygen and titanium results provided in the supporting information, Fig. S3), both Cu_{2.1}TMS and Cu_{8.5}TMS exhibit highly dispersed copper. However, Cu_{2.1}TMS does not exhibit copper aggregation on the TiO₂ surface, indicating overloaded copper formation of the isolated copper-oxide nanoparticles on the material surface [33]. This is considered Cu(II) ion invasion into the TiO₂ framework, leading to TiO₂ structure distortion. Further evidence is presented in the ex-situ XAS analysis in Section 3.2.

3.2. Raman peak information

In the Raman spectrum results depicted in Fig. 4, characteristic peaks are observed at 144, 197, 394, 514, and 636 cm⁻¹, which are assigned to the E_{g(1)}, E_{g(2)}, B_{1g}, A_{1g}, and E_{g(3)} active modes of the typical anatase TiO₂ phase, respectively [44]. The E_g-type bands predominantly signify the symmetric stretching vibration of O-Ti-O, whereas the B_{1g} band arises from the symmetric bending vibration of O-Ti-O, and the A_{1g} mode results from the antisymmetric bending vibration of O-Ti-O in TiO₂ [45]. Notably, in all types of vibration modes, the vibrational peak

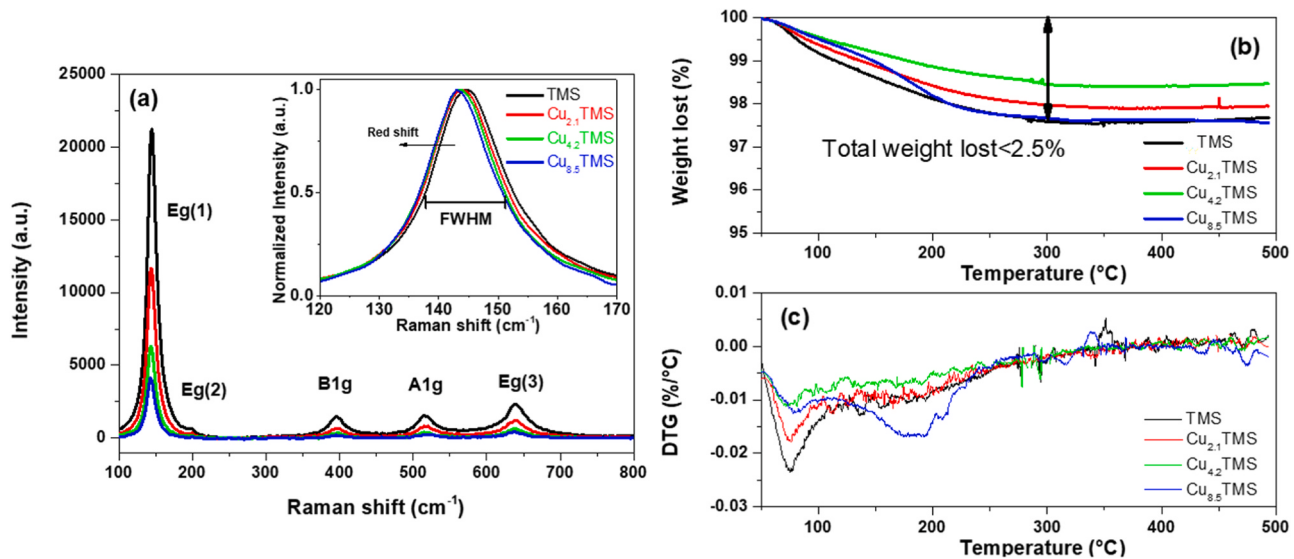


Fig. 4. Raman spectra of undoped TiO_2 and CuTMS nanoparticles (a). The inset image is the detail of the $E_{g(1)}$ mode, normalized with the sample maximum intensity. Thermogravimetric analysis (b) and differential thermal analysis (c).

intensity decreased dramatically as the copper content increased, with even the $E_{g(2)}$ vibration mode vanishing on the sample of a material with high copper loading, which may confirm that the disorder of the anatase phase is due to the introduction of copper ions into the TiO_2 framework [46]. In addition, Fig. 4(a) includes an inset image of the normalized main vibration mode of $E_{g(1)}$, where the peak shifts to a lower wave-number [35,47,48]. Furthermore, broadening of the full width at half maximum (FWHM) with respect to a smaller grain size was observed [33,49,50]. Detailed peak information and further evaluation of each vibration mode are summarized in Table 2.

Moreover, even in CuTMS with a higher copper content, the characteristic peak of copper oxide species was not observed in the Raman analysis. This is attributed to the Jahn–Teller effect, whereby copper introduced into the TiO_2 lattice structure simultaneously enhances the generation of oxygen vacancies [51–53]. The presence of transition metals such as copper in the octahedral structure typically results in distortion of the structure along the z-axis [51]. Details regarding the Raman peak intensity ratios of CuTMS are summarized in Table S2. Meanwhile, different Raman vibration peak ratios could be assigned to anatase crystal facets, in which the peak ratios of A_{1g}/E_{g1} and A_{1g}/E_{g3} were related to the crystal facets of {101} and {001}, respectively [36]. In this study, we adopted a novel approach to estimate the anatase crystal facets using the anatase Raman vibration area ratio shown in Table 2. The results for the different copper-doping amounts in the CuTMS anatase crystal facets were approximately equal. In addition, further measurement of the exposure percentage of {001} facets was conducted, yielding values of approximately 15%–17.5% across all CuTMS samples. This evidence consistently confirms that the absence of copper oxide is attributed to the introduction of copper into the TiO_2

framework. Consequently, copper doping contributes to the reduction of anatase long-range order, facilitating the formation of structural defects in CuTMS.

To verify that the structural distortion resulting from copper intrusion into the TiO_2 framework did not affect the thermal stability of CuTMS as a thermal catalyst for catalytic CO oxidation, TGA and DTG were conducted. Figs. 4(b) and 4(c) illustrate that the as-synthesized CuTMS exhibits moderate weight loss in the temperature range of $<300^\circ\text{C}$, which can be attributed to the dehydration of physically adsorbed water and the chemisorption of water. Notably, the total weight loss remained below 2.5% in all cases of CuTMS up to 500°C , indicating the high thermal stability of CuTMS. The thermal stability of CuTMS may be attributed to the strong metal–support interactions resulting from the formation of Cu–O–Ti structures [54,55].

3.3. Atomic and electronic structures of CuTMS

An XAS study was conducted to reveal the atomic structure and chemical state of the Cu species in Cu_xTMS . For the Cu K-edge, the dipole transition involves $1\text{s}\rightarrow 4\text{p}$. The quadrupole transition $1\text{s}\rightarrow 3\text{d}$ also occurs if vibrational or structural inversion symmetry exists, such as $3\text{d}^9\text{ Cu}^{2+}$ ion [56]. Fig. 5(a) presents the Cu K-edge XANES spectra of CuTMS with different Cu doping levels and reference bulk CuO and Cu_2O . The spectral features can be characterized more clearly by the first derivative of the Cu K-edge XANES, as shown in Fig. 5(b). The main peak corresponds to the edge energy for the reference compounds CuO (Cu^{2+} in a square-planar symmetry) and Cu_2O (Cu^+ coordinated by two oxygen atoms), appearing at 8983.5 and 8980 eV, respectively. The derivative spectra feature of CuTMS shows a large difference, and it is difficult

Table 2

The summary of Raman peak information: positions, intensity and full width at half maximum (FWHM) observed in the as-synthesized CuTMS.

Sample	$E_{g(1)}$ mode			B_{1g} mode	A_{1g} mode	$E_{g(3)}$ mode	$A_{1g}/E_{g(1)}^a$	$A_{1g}/E_{g(3)}^b$	{001}c
	Position (cm^{-1})	FWHM (cm^{-1})	Area (a.u.)						
TMS	144.7	14.5	413110.2	26362.6	32445.4	86630.0	7.85	37.45	17.34
$\text{Cu}_{2.1}\text{TMS}$	144.0	14.4	230605.4	13138.4	19326.7	42743.2	8.38	45.22	15.64
$\text{Cu}_{4.2}\text{TMS}$	143.5	14.0	116745.1	8732.0	9517.9	24712.5	8.15	38.51	17.47
$\text{Cu}_{8.5}\text{TMS}$	143.2	13.9	76518.1	3567.2	6600.4	14689.3	8.63	44.93	16.11

^a The Raman peak area ratio assign to the anatase {101} crystal facet.

^b The Raman peak area ratio assign to the anatase {001} crystal facet.

^c The estimate of the percentage of {001} in anatase crystal facets: {001}/({001}+{101})*100%.

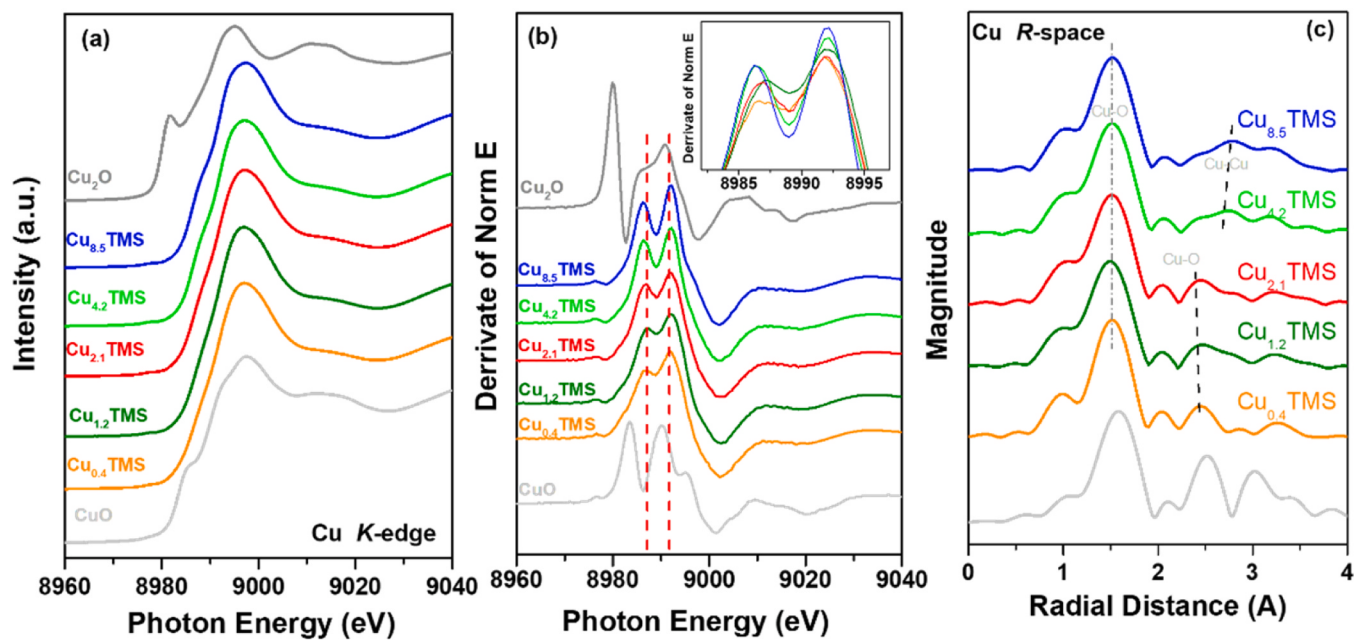


Fig. 5. Cu K-edge of bulk CuO, Cu₂O, and Cu_xTMS for (a) the XANES spectra and (b) the first derivatives of XANES spectra. (c) Fourier transform of the EXAFS in R space. Inset (b) shows the quadrupole transition features variation.

to assign it to bulk CuO or Cu₂O. The rising edge of CuTMS is shifted upward by approximately 3.5 eV compared with that of bulk CuO, but it roughly coincides with that of bulk Cu(OH)₂ (Cu²⁺ in an octahedra symmetry) [57–59]. In a previous study, TMS was demonstrated as an anatase structure, which means that the Ti⁴⁺ in TiO₂ is arranged in an octahedral symmetry. The obvious XAS evidence suggests that the incorporated Cu²⁺ possibly doped into Ti⁴⁺sites in octahedral coordination during the AASA procedure. Notably, a pre-edge feature located around 8977 eV exists for all CuTMS samples, suggesting that the quadrupole transition 1s→3d can be observed and that empty d states are available in these samples. Because the 3d¹⁰ electronic configuration of the Cu¹⁺ ion prohibits such a transition, it is concluded that the copper ions in this sample are predominantly Cu²⁺.

The substitution of Cu²⁺ for Ti⁴⁺ in octahedral coordination can influence the original octahedral symmetry through Cu-O bonding at Ti⁴⁺sites. EXAFS data were collected for both bulk CuO and CuTMS to elucidate the local structure around the Cu atom. Fourier transforms of the EXAFS, focusing on radial distances up to 4 Å, are depicted in Fig. 5 (c). Notably, the first shell of CuTMS, indicative of Cu-O coordination, appears shorter than bulk CuO and even surpasses the original first shell Ti-O bonding in TiO₂. This shorter Cu-O distance signifies the formation of Cu species within a distinct local structure, leading to a site-distorted octahedral symmetry. Differences emerge in the FTs for low-Cu-doped CuTMS (Cu_{0.4}TMS, Cu_{1.2}TMS, and Cu_{2.1}) compared with high-Cu-doped CuTMS (Cu_{4.2}TMS and Cu_{8.5}), particularly evident in the FT feature from 2.2 to 3 Å. Notably, the absence of Cu-Cu bonding in low-Cu-doped CuTMS suggests highly and atomically dispersed Cu²⁺ species in the anatase structure. However, with increasing Cu content, a peak attributed to Cu-Cu bonding emerged around 2.9 Å, indicating the formation of Cu oxide clusters. Integrating XANES and EXAFS results in Fig. 5, it becomes apparent that in addition to well-dispersed Cu species in octahedral symmetry, microcrystalline CuO clusters are likely formed for Cu doping contents exceeding 4.2 wt%. This observation suggests an increase in the fraction of Cu oxide clusters with increasing Cu content, representing the dominant pathway for Cu growth.

3.4. CuTMS oxygen supplementation investigation

Surface chemical adsorption analysis of materials can be a powerful

strategy for unraveling information about heterogeneous reactions. The designed CO-TPR/O₂-TPO process can not only aid in comprehending the surface reduction ability of CuTMS but also provide insights into oxygen resupply on the catalyst surface. In Fig. 6(a), the CO-TPR results indicate no obvious CO consumption below 600°C for the undoped TMS material, with a minor production of CO₂ at ~650°C, as depicted in Fig. 6(b). Conversely, CuTMS exhibits three CO reduction peaks across all copper-loaded samples, located at approximately 150°C, 450°C, and 700°C. After CO consumption, the relative CO₂ formation peaks are also observed in Fig. 6(b). Based on these observations, peaks I and II at 150°C and 450°C, respectively, can be assigned to two types of active copper sites, while the third peak is associated with TiO₂ reduction. Notably, the absence of reduction peak II in the Cu_{2.1}TMS sample is intriguing and closely correlates with its surface, which is characterized by the absence of isolated copper-oxide nanoparticle species. This observation strongly aligned with the ex-situ XAS analysis presented in Section 3.2. Consequently, peak I can be assigned to the Cu-O-Ti type of copper species, which is consistently observed across all copper-loaded samples. Peak II in CO consumption is associated with copper oxide nanoparticles present on the CuTMS surface. The inset graph in Fig. 6(b) illustrates the oxygen contribution from TiO₂ lattice oxygen (peak III). Remarkably, the amount of CO₂ formation follows the order: Cu_{2.1}TMS > Cu_{4.2}TMS > Cu_{8.5}TMS ≈ TMS, which contrasts with the catalytic CO ability. This lower CO₂ production is attributed to the varying self-contributing lattice oxygen ability of CuTMS, with the order being Cu_{8.5}TMS > Cu_{4.2}TMS > Cu_{2.1}TMS >> TMS, emanating from the Cu-O-Ti type of active site. Notably, the peak I region active site (Cu-O-Ti) exhibited more self-CO oxidation activity compared to peak II (isolated copper) against the CO consumption temperature. Consequently, in the subsequent section we solely focus on the dominant Cu-O-Ti active site and its contribution to overall CuTMS catalytic CO oxidation.

Furthermore, O₂-TPR experiments were conducted immediately after CO-TPR, and the CuTMS material used after CO-TPR analysis was not exposed to the atmosphere for monitoring the CuTMS oxygen supplement ability [22]. TMS exhibited a negligible amount of CO₂ formation, which is possibly attributed to adsorbed carbon species remaining on the TMS surface, as shown in Figs. 6(c) and 6(d). Regrettably, samples of Cu_{2.1}TMS and Cu_{4.2}TMS likely experienced damage to their natural properties due to the high CO reduction

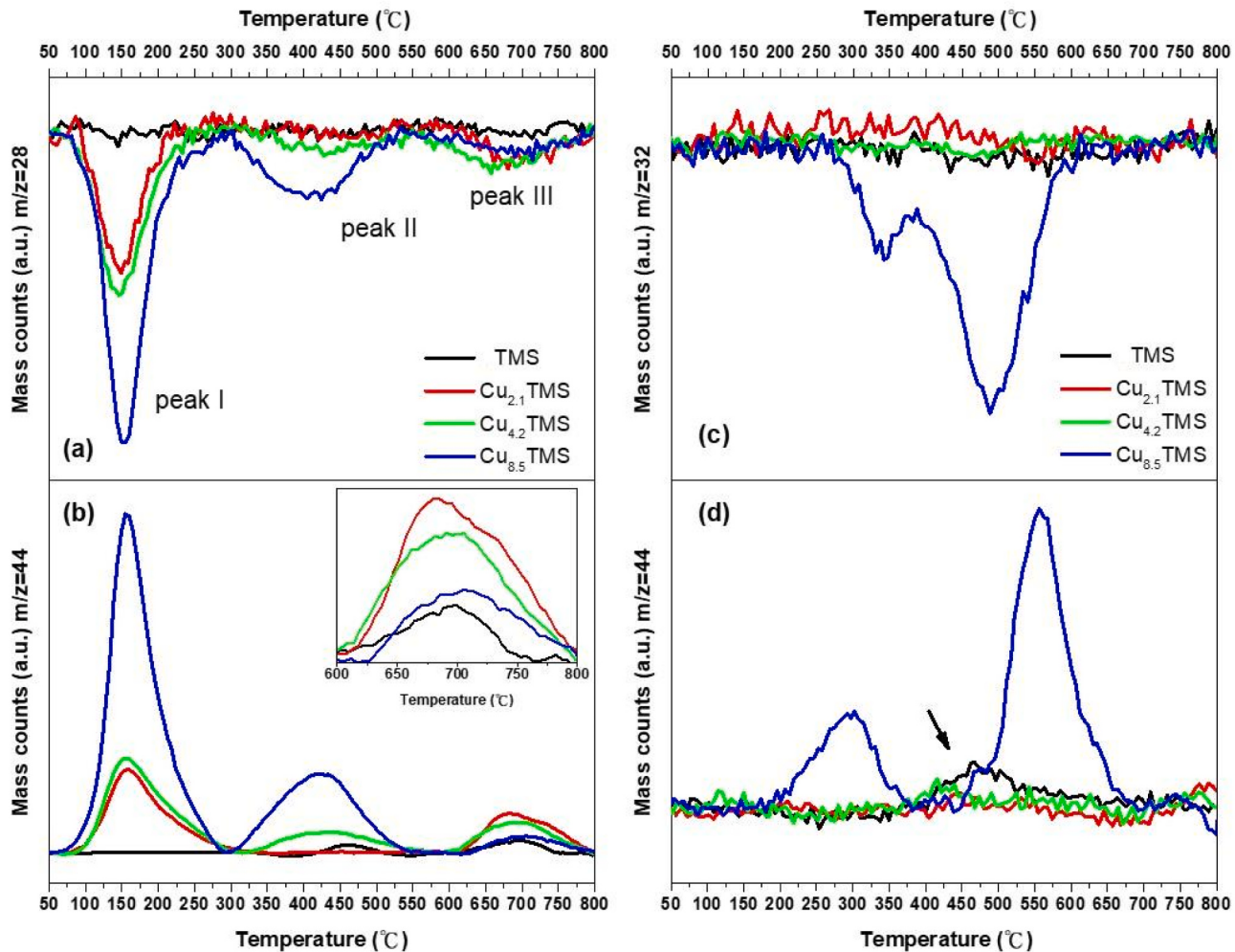


Fig. 6. The real-time mass results of CO-TPR (a) the CO consumption and (b) the formation of CO_2 ; the CuTMS O_2 -TPO analysis for re-oxidation ability test after CO-TPR, the oxygen consumption (c) and the related CO_2 formation(d) (4%CO:96%Ar=15 ml/min for CO-TPR and O_2 -TPO were carry out under 4% O_2 :96%Ar=15 ml/min, ramp= 2 $^{\circ}\text{C}/\text{min}$).

temperature, as illustrated in Fig. 6(d). Fortunately, $\text{Cu}_{8.5}\text{TMS}$ not only consumes oxygen but also eliminates the remaining carbon species in the presence of oxygen in the atmosphere. Notably, oxygen consumption surpasses the relative CO_2 formation. This phenomenon indicates that there are some oxygen supplements for oxygen vacancies, which can be potentially attributed to the strong redox ability and thermal stability provided by the Cu-O-Ti structure.

The findings from the abovementioned CO-TPR and oxygen resupply suggest that the Cu-O-Ti active site possesses the capability to drive CO oxidation even in the absence of oxygen using the TiO_2 lattice oxygen. Consequently, the actual CO oxidation process occurs in an oxygen-rich environment (1%CO:1% O_2), where catalytic CO oxidation predominantly occurs on Cu-O-Ti active sites. This phenomenon arises from TiO_2 contributing its lattice oxygen while generating oxygen vacancies. These vacancies subsequently reoxidize by absorbing O_2 from the reaction gas.

3.5. In-situ XAS and operando Raman for evaluating catalytic mechanism

The CuTMS catalytic CO oxidation operando Raman spectra were obtained across the entire range from 100 to 3500 cm^{-1} , with the output reaction gases from the heating stage concurrently monitored by a tandem real-time mass spectrometer, as illustrated in Fig. S4. Different ranges of the Raman spectrum can be assigned to specific vibration features, which enables the identification of specific regions: I. Within the range of 100–800 cm^{-1} , which is the catalytic CO oxidation

influence range on anatase TiO_2 characteristic vibration. II. The vibration around 700–1000 cm^{-1} , which can be assigned to the C-O bond vibration mode. III Observation of carbon species generated during CO oxidation (1150–2500 cm^{-1}).

I. The CuTMS catalytic CO oxidation operando Raman results are depicted through a series of three-dimensional (3D) surface plots in Fig. 7(a)–(d) for TMS, $\text{Cu}_{2.1}\text{TMS}$, $\text{Cu}_{4.2}\text{TMS}$, and $\text{Cu}_{8.5}\text{TMS}$. For better vision the detail information of the vibration mode of B_{1g} , A_{1g} and $\text{E}_{g(3)}$, the contour map image were provided in S.I. (Fig. S5) This finding corroborates the CuTMS catalytic CO oxidation described in Section 3.1; notably, undoped TMS exhibits minimal changes during the catalytic CO oxidation process across all types of anatase vibration modes. The integrated anatase TiO_2 main Raman characteristic peak $\text{E}_{g(1)}$ is presented in Fig. 7(e), which represents the normalized peak intensity related to the peak intensity at 50 $^{\circ}\text{C}$. Regarding the TMS CO oxidation operando Raman result, the effect of heating and laser was no longer our focus. Remarkably, all copper-doped CuTMS samples exhibited significant intensity variations closely linked to the reaction temperature. The integrated $\text{E}_{g(1)}$, B_{1g} , A_{1g} , and $\text{E}_{g(3)}$ Raman shifts are depicted in Figs. 7(f) and 7(g). Notably, the $\text{E}_{g(1)}$ mode of the Raman vibration shifted to a higher wavelength during CO oxidation. However, the bands of A_{1g} and $\text{E}_{g(3)}$ demonstrated a behavior opposite to that of the $\text{E}_{g(1)}$ mode,

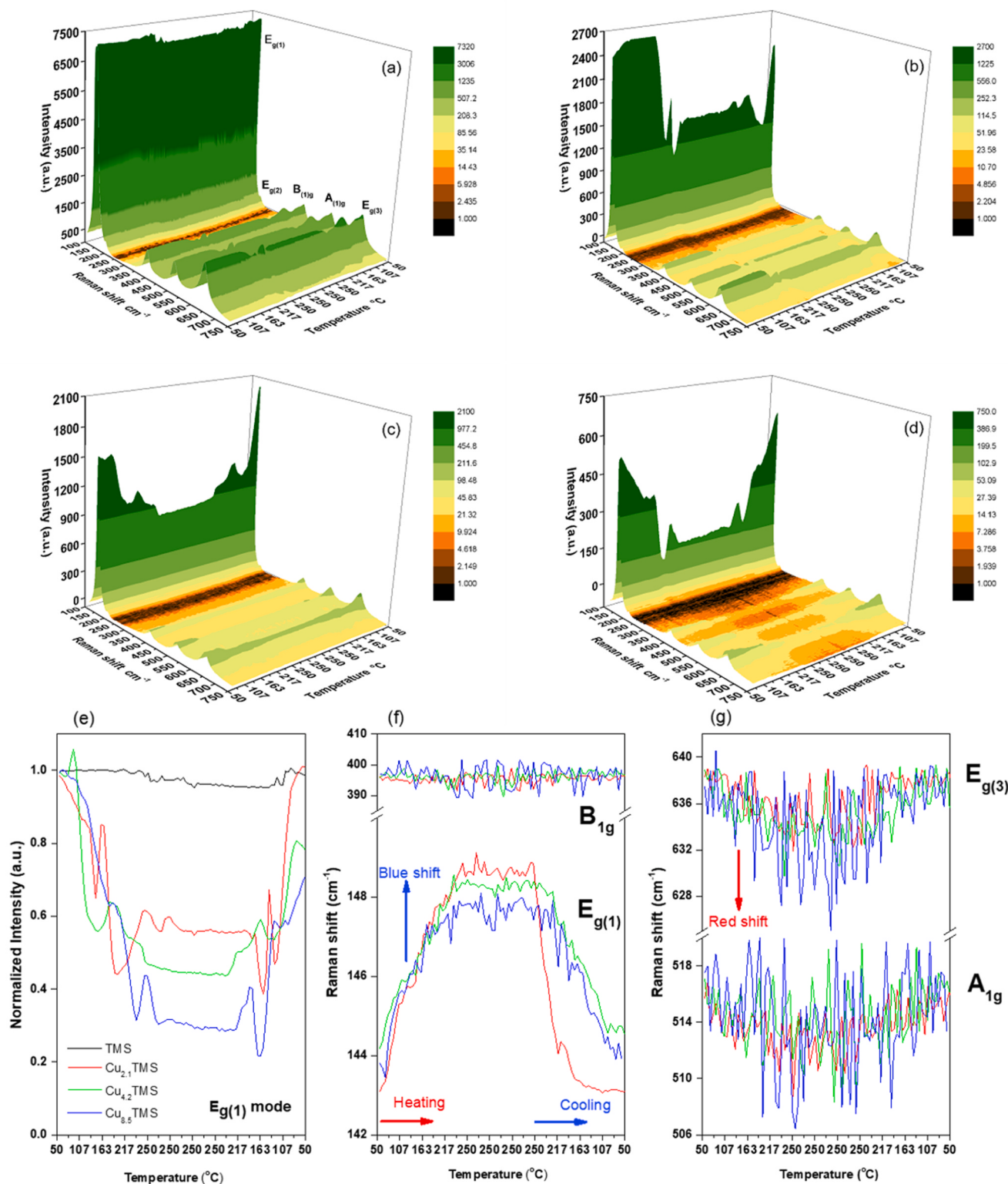


Fig. 7. The operando Raman spectrum of catalytically CO oxidation 3D Surface Plots of (a) TMS, (b)Cu_{2.1}TMS, (c) Cu_{4.2}TMS and (d) Cu_{8.5}TMS; the peak integration of different vibration band (e) Normalized peak intensity of E_{g(1)}, (f) peak position of E_{g(1)} and B_{1g}, (g) the A_{1g} and E_{g(3)}. The reaction conditions were settled as catalytic CO oxidation.

indicating the formation of a defect structure during the reaction [51]. Additionally, the Cu_{2.1}TMS E_{g(1)} peak shifts healed, where the peak shift dropped back faster than Cu_{4.2}TMS and Cu_{8.5}TMS, indicating a faster disappearance of the defect structure. This

finding aligns with the CuTMS catalytic CO oxidation shown in Fig. 2.

II. In Figs. 8(a) and 8(b), a weak broadening vibration feature is observed around 800 cm⁻¹; this band is commonly assigned to the asymmetric stretching vibration of the C-O bond in the

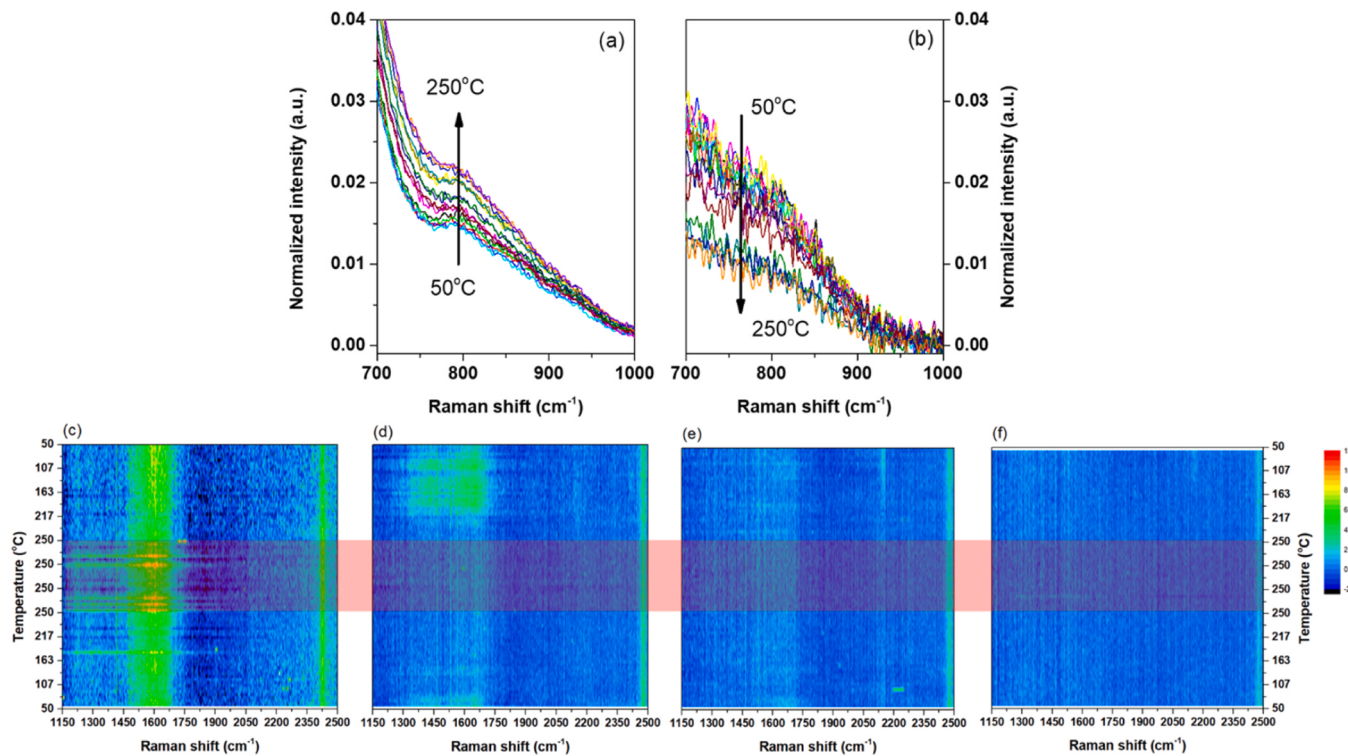


Fig. 8. (a) and (b) the Raman spectra of $\sim 800\text{ cm}^{-1}$ mode recording with rising the reaction temperature of TMS and Cu_{8.5}TMS; (c) to (e) the contour plots of operando Raman spectra during the CO oxidation for TMS, Cu_{2.1}TMS, Cu_{4.2}TMS, and Cu_{8.5}TMS, respectively.

carbonate group [60]. Consequently, CO can be adsorbed onto the CuTMS surface. Thus, the C-O bond behaves in different ways in response to TMS and Cu_{8.5}TMS. TMS exhibits an increase in the C-O bond as the reaction temperature increases, consistent with the CO-TPR results. Conversely, Cu_{8.5}TMS demonstrates the disappearance of the C-O bond as the reaction temperature increases, potentially explaining the removal of CO on the CuTMS surface illustrated in Fig. 8(b).

III. In Figs. 8(c) and 8(f), additional carbon species are also observed in the three regions. First, both TMS and Cu_{2.1}TMS occupy the band located at 1600–1650 cm⁻¹ assigned to the C-C stretch mode and C-C double bond, which are generally representative amorphous carbon species [61–63]. However, this bond is almost undetectable on the catalysts of Cu_{4.2}TMS and Cu_{8.5}TMS with higher CO oxidation performance (higher copper content). Secondly, a small amount of vibration features around 1400–1500 cm⁻¹ attributed to the C-C [64] or C-O [65] stretching mode only appears for Cu_{2.1}TMS. This type of vibration band does not exist in Cu_{4.2}TMS or Cu_{8.5}TMS.

Lastly, there is a relatively sharper peak with stable existence at 2450 cm⁻¹ in all samples. This band indicates the presence of defective carbon structure (D+D' mode) [66,67]. Overall, this observation reveals that no significant accumulation of carbon species occurs on the CuTMS surface.

In summary, TMS primarily exhibits CO adsorption behavior, whereas the Cu_{2.1}TMS behavior includes carbon species-removal ability similar to its CO oxidation capability. Consequently, catalysts with higher copper loading, such as Cu_{4.2}TMS and Cu_{8.5}TMS, exhibit dramatically different CO adsorption and removal behavior compared to Cu_{2.1}TMS and TMS. Notably, the anatase structure changed like an elastic material in the operando Raman observations; this finding is strongly corroborated by 3D strain dynamics studies [39,40], which identified material defect formation associated with reaction temperature. The operando Raman monitoring result is one of the most

important techs applied for observing the crystal facets ration changes. For comparison, the selected Raman spectrum were provided which is the catalytic CO oxidation ramping procedural for every 50 °C in Fig. S6. As previously mentioned, the operando Raman peak intensity ratio is illustrated in Fig. S7. Further analysis of the operando Raman peak area ratio for estimating changes in anatase facets is summarized in Fig. 9. Fig. 9(a) presents the integrated characteristic Raman peak area ratio alongside the estimated {001} facet ratio from Table 2 for comparison. The bar chart in Fig. 9(a) indicates no significant changes between the different CuTMSs. However, Fig. 9(b) reveals a slight decrease in both CuTMS crystal facets of {101} and {001} with increasing catalytic CO oxidation temperature. In Fig. 9(c), the estimated {001} facet ratio changes with catalytic CO oxidation, revealing changes in the anatase structure [36]. The illustrations reveal the distortion of the CuTMS anatase structure along the z-axis, resulting in a reduction in the {001} facet ratio from the initial CO oxidation (@50°C) of almost 17–10% at 250°C. Importantly, the as-prepared CuTMS could completely heal during the cooling procedure, indicating the resupply of TiO₂ lattice oxygen. These observations align with the material CO oxidation results depicted in Fig. 2, where CuTMS exhibits CO oxidation hysteresis behavior.

While the operando Raman observations provide insights into the potential reaction mechanism in the high-temperature region, the reaction triggering off CuTMS catalytic CO oxidation at 150°C is still inexplicable. To reveal a conceivable pathway for Cu_{8.5}TMS activating CO oxidation in a relatively low-temperature region, an in-situ XAS experiment was conducted to investigate the reaction mechanism and intermediate surface species. Figs. 10(b) and 10(c) display the first-derivative in-situ Cu K-edge XANES spectra over the temperature range of 40°C–130°C (The original in-situ Cu K-edge XANES present in Fig. 10a). At the onset of Cu_{8.5}TMS catalytic CO oxidation (under 50°C), features indicative of CuO were observed, consistent with the observation result of ex-situ XANES shown in Fig. 5(a). As the temperature increased, the intensity of the peak representing the Cu(II) pre-edge decreased. Subsequently, with further heating, new features emerged

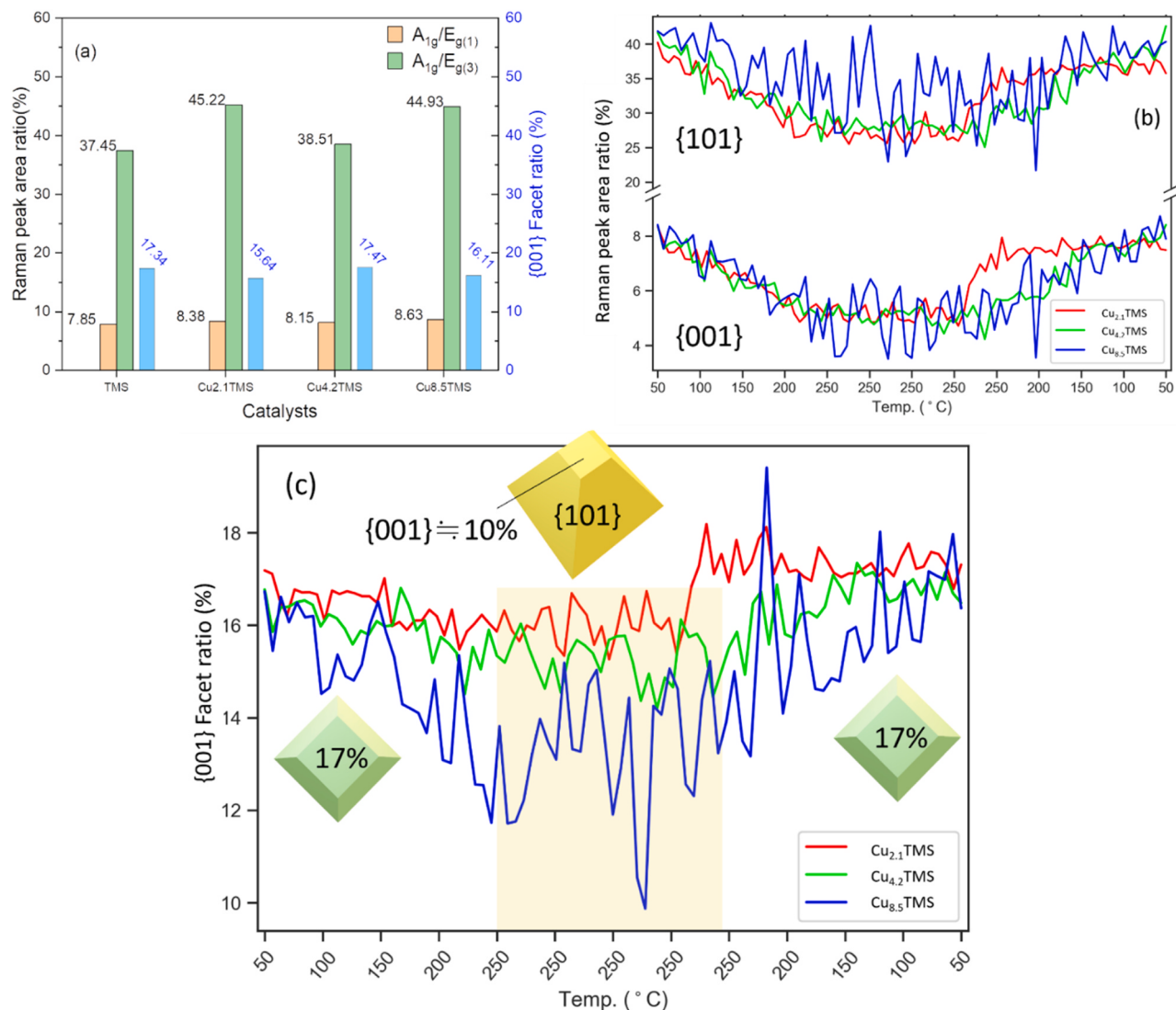


Fig. 9. (a) the characteristic Raman peak area ratio and the estimate {001} facet ratio, (b) the operando Raman peak area ratio of $A_{1g}/E_{g(1)}$, and $A_{1g}/E_{g(3)}$, (c) the estimate {001} facet ratio changes follow the catalytic CO oxidation.

around 8979–8981 eV, implying the existence of characteristics of reductive Cu species [29,68]. At that time, the predominant Cu species likely changed from CuO to a mixture of Cu₂O/CuO. This phenomenon is likely related to the improved copper dispersion and the strong copper–titanium interaction, which facilitates the easy reduction of surface copper oxides.

To understand the surface Cu species, the in-situ O K-edge in the total-electron-yield (TEY) mode was also implemented. The surface-sensitive electron signal can provide complementary information to the fluorescence (photon signal) XANES. Fig. 10 (d) depicts a plot of the in-situ XANES spectra of the Cu_{8.5}TMS catalytic CO oxidation taken at the oxygen K-edge. Initially, the spectra exhibit two maxima at 530.1 and 536.6 eV. The maximum at 530.1 eV closely aligns with the white line of CuO, which is attributed to transitions to conduction band states formed by the hybridization of O 2p with Cu 3d electrons [69]. However, the broad peak in the energy range of 535–540 eV is difficult to attribute to known copper oxides. This feature of an atomic oxygen species should be assigned to a Cu–O compound with weaker chemical bonding than in known oxides. Notably, as only one broad resonance was observed, it was assigned to a novel copper suboxide with O_{2p}Cu_{4s}p hybridization. It is rational to consider a suboxide that lacks Cu d-band interaction with this atomic species as a surface intermediate between

an oxide and a solid solution of oxygen atoms in a Cu matrix [70–72]. As the temperature increases, the formation of the Cu suboxide alters the electronic structure of Cu and provides an additional oxygen species, which is directly involved in CO oxidation and functions as an activated site. Remarkably, compared with previous studies, the copper suboxide in this study could be observed in a much lower temperature region, consistent with the activation temperature of Cu_{8.5}TMS [29,68,73]. This characteristic of the high-Cu-loading sample can be attributed to the formation of a stronger covalent Cu–O bond in the Cu matrix, as indicated by the downward shift of the dipole transition feature (inset of Fig. 5(b)) [56]. Up to temperatures of 60°C, the suboxide feature occurred with both CuO and Cu₂O absorption edges at 530.1 and 532.5 eV, respectively. However, with further increase in temperature, the features of Cu₂O became predominant in the O K-edge XANES spectra until 110°C, indicating the presence of Cu(I) as a reactive species on the surface. Subsequently, a mixture of Cu₂O/CuO was observed as the main feature. The surface signal of CuO → Cu₂O → Cu₂O/Cu transformation seen in the XANES spectra is in good agreement with the mechanism for the catalytic CO oxidation reaction over heterogeneous metal-oxide systems. In the low-temperature region, surface-adsorbed oxygen, rather than lattice oxygen, is deemed to be a more plausible source of oxygen.

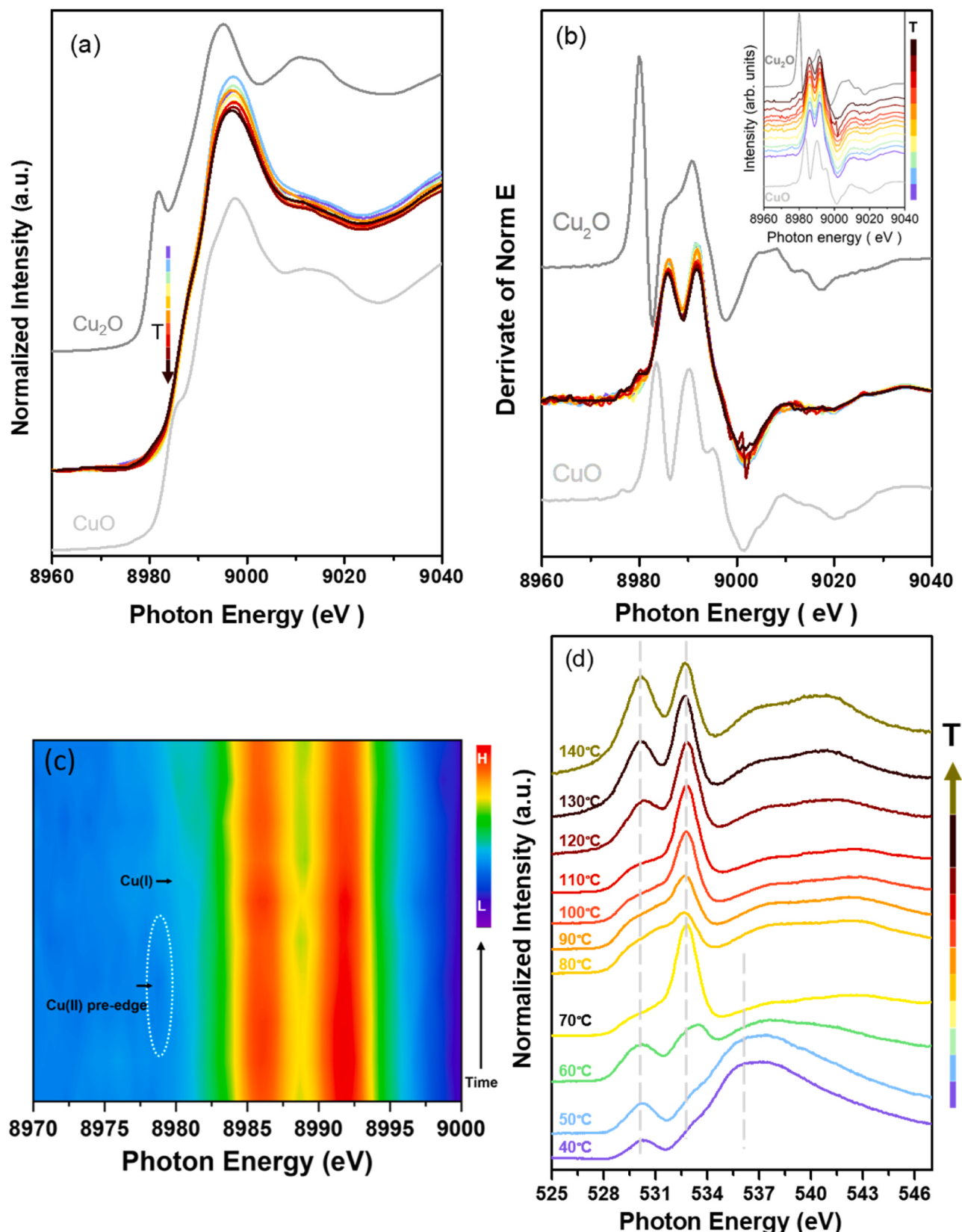


Fig. 10. Characterization of a $\text{Cu}_{8.5}\text{TMS}$ under reaction: (a) Cu K-edge XANES spectra with bulk Cu_2O and CuO and (b) the corresponding first derivative of XANES spectra, (c) contour map of first-derivative Cu K-edge XANES spectra, (d) O K-edge XANES spectra. Inset (b) shows individual first derivative Cu K-edge XANES spectra while increasing temperature.

4. Conclusion

Coupling in-situ XAS and operando Raman facilitates the monitoring of copper-doped TiO_2 for CO oxidation across different working temperatures and activation modes. CO oxidation could be activated at relatively low temperatures because copper suboxides form on the surface of copper as an intermediate species, which easily absorbs oxygen to form a catalytic cycle. Operando Raman revealed anatase vibration mode variation, including Raman shifts, peak intensity, FWHM, and peak area, all of which indicate structural distortion with reaction temperature. The peak area used to estimate the anatase structure during catalytic CO oxidation of crystal facets of {101} and {001} changes, which is the reason for the hysteresis behavior. This study provides direct in-situ and operando evidence for oxygen replenishment behavior during CO oxidation. Understanding this mechanism could potentially enhance CO reformation and water gas shift reactions in the future.

CRediT authorship contribution statement

Li Cheng Kao: Writing – review & editing, Writing – original draft, Validation, Data curation, Conceptualization. **Xian-Teng Yu:** Software, Methodology, Data curation. **Wen-Ta Yang:** Writing – original draft, Methodology, Investigation, Formal analysis, Data curation. **Chung-Li Dong:** Resources, Project administration, Conceptualization. **Sofia Ya Hsuan Liou:** Funding acquisition, Conceptualization.

Declaration of Competing Interest

The authors declare that they have no known competing financial interests or personal relationships that could have appeared to influence the work reported in this paper.

Data availability

No data was used for the research described in the article.

Acknowledgements

This work is financially supported by the National Science and Technology Council, Taiwan (Contract no: 112-2116-M-002-009 and 112-2116-M-006-015-), and the Research Center for Future Earth from the Featured Areas Research Center Program within the Higher Education Sprout Project framework by the Ministry of Education Republic of China (Taiwan). The authors are grateful for the support from the beamline staff at BL17C and BL20A at Taiwan Light Source, and the support from Dr. Yu-Cheng Shao at BL12B2 at Spring-8.

Appendix A. Supporting information

Supplementary data associated with this article can be found in the online version at [doi:10.1016/j.apcatb.2024.124017](https://doi.org/10.1016/j.apcatb.2024.124017).

References

- Zinoviev, F., Müller-Langer, P., Das, N., Bertero, P., Fornasiero, M., Kaltschmitt, G., Centi, S., Miertus, Next-generation biofuels: survey of emerging technologies and sustainability issues, *ChemSusChem* 3 (2010) 1106–1133.
- Weng, S.-F., Hsieh, H.-C., Lee, C.-S., Hydrogen production from oxidative steam reforming of ethanol on nickel-substituted pyrochlore phase catalysts, *Int. J. Hydrog. Energy* 42 (2017) 2849–2860.
- Ramos, I.A.C., Montini, B., Lorenzut, H., Troiani, F.C., Gennari, M., Graziani, P., Fornasiero, Hydrogen production from ethanol steam reforming on $\text{M}/\text{CeO}_2/\text{YSZ}$ ($\text{M}=\text{Ru, Pd, Ag}$) nanocomposites, *Catal. Today* 180 (2012) 96–104.
- De Rogatis, T., Montini, B., Lorenzut, P., Fornasiero, NixCu y /Al 2O_3 based catalysts for hydrogen production, *Energy Environ. Sci.* 1 (2008) 501–509.
- Houston, R., Labb  , D., Hayes, C.S., Daw, N., Abdouloumouine, Intermediate temperature water-gas shift kinetics for hydrogen production, *React. Chem. Eng.* 4 (2019) 1814–1822.
- Wang, L.C., Widmann, D.J., Behm, Reactive removal of surface oxygen by H_2 , CO and CO/H_2 on a Au/CeO_2 catalyst and its relevance to the preferential CO oxidation (PROX) and reverse water gas shift (RWGS) reaction, *Catal. Sci. Technol.* 5 (2015) 925–941.
-   wka, K., Czelej, J.C., Colmenares, K., Jablczy  ska, L., Werner, L., Grado  , Supported plasmonic nanocatalysts for hydrogen production by wet and dry photoreforming of biomass and biogas derived compounds: recent progress and future perspectives, *ChemCatChem* 13 (2021) 4458–4496.
- Cui, X., Yu, H.-Y., Chen, R., Chen, L., Yu, J., Dong, C., Ma, S., Wang, J., Li, F., Yang, J., Xiao, M., Zhang, D., Ma, D., Deng, D.H., Zhang, Z., Tian, X., Bao, Room-temperature electrochemical water-gas shift reaction for high purity hydrogen production, *Nature Commun.* 10 (2019) 86.
- Haruta, M., Kobayashi, T., Sano, N., Yamada, Novel gold catalysts for the oxidation of carbon monoxide at a temperature far below 0 °C, *Chem. Lett.* 16 (1987) 405–408.
- Zhang, X., Zhang, L., Song, F., Hou, Y., Yang, Y., Wang, N., Liu, Enhanced catalytic performance for CO oxidation and preferential CO oxidation over CuO/CeO_2 catalysts synthesized from metal organic framework: effects of preparation methods, *Int. J. Hydrog. Energy* 43 (2018) 18279–18288.
- Tang, X., Wang, J., Li, X., Zhang, P., La, X., Jiang, B., Liu, In-situ growth of large-area monolithic $\text{Fe}_2\text{O}_3/\text{TiO}_2$ catalysts on flexible Ti mesh for CO oxidation, *J. Mater. Sci. Technol.* 69 (2021) 119–128.
- Cai, Y., Xu, J., Guo, J., Liu, Ultrathin, polycrystalline, two-dimensional Co_3O_4 for low-temperature CO oxidation, *ACS, ACS Catal.* 9 (2019) 2558–2567.
- Mo, S., He, H., Ren, S., Li, W., Zhang, M., Fu, L., Chen, J., Wu, Y., Chen, D., Ye, Macroporous Ni foam-supported Co_3O_4 nanobrush and nanomace hybrid arrays for high-efficiency CO oxidation, *J. Environ. Sci.* 75 (2019) 136–144.
- Schubert, M., Hackenberg, S., van Veen, A.C., Muhler, M., Plzak, R.J., Behm, CO Oxidation over supported gold catalysts—“inert” and “active” support materials and their role for the oxygen supply during reaction, *J. Catal.* 197 (2001) 113–122.
- Kotobuki, M., Leppelt, R., Hansgen, D., Widmann, R.J., Behm, Reactive oxygen on a Au/TiO_2 supported catalyst, *J. Catal.* 264 (2009) 67–76.
- Newton, M.A., Ferri, G., Smolentsev, V., Marchionni, M., Nachtegaal, Room-temperature carbon monoxide oxidation by oxygen over $\text{Pt}/\text{Al}_2\text{O}_3$ mediated by reactive platinum carbonates, *Nature, Communications* 6 (2015) 8675.
- Kim, G.J., Lee, S.M., Chang Hong, S.S., Kim, Active oxygen species adsorbed on the catalyst surface and its effect on formaldehyde oxidation over Pt/TiO_2 catalysts at room temperature; role of the Pt valence state on this reaction? *RSC Adv.* 8 (2018) 3626–3636.
- Luo, L., Nian, S., Wang, Z., Dong, Y., He, Y., Han, C., Wang, Real-time atomic-scale visualization of reversible copper surface activation during the CO oxidation reaction, *Angew. Chem. Int. Ed.* 59 (2020) 2505–2509.
- Zhang, C., Wang, B., Hellman, M., Shipilin, A., Schaefer, L.R., Merte, S., Blomberg, X., Wang, P.-A., Carlsson, E., Lundgren, J., Weissenrieder, A., Resta, A., Mikkelsen, J., Andersen, J., Gustafson, S., Steps and catalytic reactions: CO oxidation with preadsorbed O on Rh(553), *Surf. Sci.* 715 (2022) 121928.
- Zhang, X.-m., Tian, P., Tu, W., Zhang, Z., Xu, J., Han, Y.-F., Tuning the dynamic interfacial structure of copper-ceria catalysts by indium oxide during CO oxidation, *ACS Catal.* 8 (2018) 5261–5275.
- Wei, X., Shao, Y., Zhou, Y., Li, C., Jin, J., Liu, W., Shen, Geometrical structure of the gold–iron(III) oxide interfacial perimeter for CO oxidation, *Angew. Chem. Int. Ed.* 57 (2018) 11289–11293.
- Gu, L., Su, Q., Jiang, W., Yao, Y., Pang, W., Ji, C.-T., Au, How do the unique $\text{Au}/\alpha\text{-Fe}_2\text{O}_3$ interfacial structures determine activity in CO oxidation? *Catal. Sci. Technol.* 8 (2018) 5782–5793.
- Ro, I., Aragao, I.B., Chada, J.P., Liu, Y., Rivera-Dones, K.R., Ball, M.R., Zanchet, J., Dumesic, J.A., Huber, G.W., The role of $\text{Pt}-\text{Fe}_x\text{O}_y$ interfacial sites for CO oxidation, *J. Catal.* 358 (2018) 19–26.
- Wang, P., Ren, J., Hu, Y., Tu, Z., Gong, Y., Cui, Y., Zheng, M., Chen, W., Zhang, C., Ma, L., Yu, F., Yang, Y., Wang, X., Bao, D., Deng, Electron penetration triggering interface activity of Pt-graphene for CO oxidation at room temperature, *Nat. Commun.* 12 (2021) 5814.
- Lee, Y., He, G., Akey, A.J., Kkey, R., Si, M., Flytzani-Stephanopoulos, I.P., Herman, R., Raman analysis of mode softening in nanoparticle $\text{CeO}_2-\delta$ and $\text{Au}-\text{CeO}_2-\delta$ during CO oxidation, *J. Am. Chem. Soc.* 133 (2011) 12952–12955.
- Liu, H.-H., Wang, Y., Jia, A.-P., Jia, S.-Y., Wang, M.-F., Luo, J.-Q., Lu, Oxygen vacancy promoted CO oxidation over Pt/CeO_2 catalysts: a reaction at Pt–CeO₂ interface, *Appl. Surf. Sci.* 314 (2014) 725–734.
- Yang, J., Hu, Y., Fang, S., Hoang, L., Li, W., Yang, Z., Liang, J., Wu, J., Hu, W., Xiao, C., Pan, Z., Luo, J., Ding, L., Zhang, Y., Guo, Oxygen vacancy promoted O₂ activation over perovskite oxide for low-temperature CO oxidation, *ACS Catal.* 9 (2019) 9751–9763.
- Wang, Y.-G., Cantu, D.C., Lee, M.-S., Li, J., Li, V.-A., Glezakou, R., Rousseau, CO oxidation on Au/TiO_2 : condition-dependent active sites and mechanistic pathways, *J. Am. Chem. Soc.* 138 (2016) 10467–10476.
- Elias, J.S., Stoerzinger, K.A., Hong, W.T., Risch, M., Giordano, A.N., Mansour, Y., Shao-Horn, In situ spectroscopy and mechanistic insights into CO oxidation on transition-metal-substituted ceria nanoparticles, *ACS Catal.* 7 (2017) 6843–6857.
- Kim, H.J., Jang, M.G., Shin, D., Shin, J.W., Han, Design of ceria catalysts for low-temperature CO oxidation, *ChemCatChem* 12 (2020) 11–26.
- Wang, X., Jia, C., Sharman, E., Zhang, G., Li, X., Jiang, J., Carbon monoxide oxidation promoted by surface polarization charges in a CuO/Ag hybrid catalyst, *Sci. Rep.* 10 (2020) 2552.
- Yuan, L.-P., Jiang, W.-J., Jiang, X.-L., Liu, Y.-H., He, C., He, T., Tang, J., Zhang, J.-S., Hu, Molecularily engineered strong metal oxide–support interaction enables highly efficient and stable CO₂ electroreduction, *ACS Catal.* 10 (2020) 13227–13235.

[33] W.-T. Yang, C.J. Lin, T. Montini, P. Fornasiero, S. Ya, S.Y.H. Liou, High-performance and long-term stability of mesoporous Cu-doped TiO₂ microsphere for catalytic CO oxidation, *J. Hazard. Mater.* 403 (2021) 123630.

[34] Y. Zhang, Z. Xu, G. Li, X. Huang, W. Hao, Y. Bi, Direct observation of oxygen vacancy self-healing on TiO₂ photocatalysts for solar water splitting, *Angew. Chem. Int. Ed.* 58 (2019) 14229–14233.

[35] T.T. Loan, V.H. Huong, N.T. Huyen, L. Van Quyet, N.A. Bang, N.N. Long, Anatase to rutile phase transformation of iron-doped titanium dioxide nanoparticles: the role of iron content, *Opt. Mater.* 111 (2021) 110651.

[36] G. Zeng, K.-K. Li, H.-G. Yang, Y.-H. Zhang, Micro-Raman mapping on an anatase TiO₂ single crystal with a large percentage of reactive (001) facets, *Vib. Spectrosc.* 68 (2013) 279–284.

[37] M.A. Barañas, M.O. Guerrero-Pérez, J.L.G. Fierro, G.G. Cortez, Raman spectroscopy during catalytic operations with on-line activity measurement (operando spectroscopy): a method for understanding the active centres of cations supported on porous materials, *J. Mater. Chem.* 12 (2002) 3337–3342.

[38] X. Sercordel, E. Berrier, M. Capron, S. Cristol, J.-F. Paul, M. Fournier, E. Payen, TiO₂-supported rhodium oxide catalysts for methanol oxidation: effect of support texture on the structure and reactivity evidenced by an operando Raman study, *Catal. Today* 155 (2010) 177–183.

[39] A.R. Passos, A. Rochet, L.M. Manente, A.F. Suzana, R. Harder, W. Cha, F. Meneau, Three-dimensional strain dynamics govern the hysteresis in heterogeneous catalysis, *Nature, Communications* 11 (2020) 4733.

[40] F. Meneau, A. Rochet, R. Harder, W. Cha, A. Ribeiro Passos, Operando 3D imaging of defects dynamics of twinned-nanocrystal during catalysis, *J. Phys.: Condens. Matter* 33 (2021) 274004.

[41] T.-J. Ju, C.-H. Wang, S.D. Lin, Insights into the CO₂ deoxygenation to CO over oxygen vacancies of CeO₂, *Catal. Sci. Technol.* 9 (2019) 2118–2124.

[42] P.-A. Carlsson, M. Skoglundh, Low-temperature oxidation of carbon monoxide and methane over alumina and ceria supported platinum catalysts, *Appl. Catal. B: Environ.* 101 (2011) 669–675.

[43] M. Casapu, A. Fischer, A.M. Gänzler, R. Popescu, M. Crone, D. Gerthsen, M. Türk, J.-D. Grunwaldt, Origin of the normal and inverse hysteresis behavior during CO oxidation over Pt/Al2O₃, *ACS Catal.* 7 (2017) 343–355.

[44] T. Ohsaka, F. Izumi, Y. Fujiki, Raman spectrum of anatase, TiO₂, *J. Raman Spectrosc.* 7 (1978) 321–324.

[45] F. Tian, Y. Zhang, J. Zhang, C. Pan, Raman spectroscopy: a new approach to measure the percentage of anatase TiO₂ exposed (001) facets, *J. Phys. Chem. C.* 116 (2012) 7515–7519.

[46] M. Šćepanović, S. Askrabić, V. Berec, A. Golubović, Z. Dohćević-Mitrović, A. Kremenović, Z. Popović, Characterization of La-Doped TiO₂ Nanopowders by Raman Spectroscopy, *Acta Phys. Pol. A* 115 (2009) 771–774.

[47] R. Palomino-Merino, P. Trejo-García, O. Portillo-Moreno, S. Jiménez-Sandoval, S. A. Tomás, O. Zelaya-Angel, R. Lozada-Morales, V.M. Castaño, Red shifts of the Eg (1) Raman mode of nanocrystalline TiO₂:Er monoliths grown by sol-gel process, *Opt. Mater.* 46 (2015) 345–349.

[48] V.R. Akshay, B. Arun, G. Mandal, A. Chanda, M. Vasundhara, Significant reduction in the optical band-gap and defect assisted magnetic response in Fe-doped anatase TiO₂ nanocrystals as dilute magnetic semiconductors, *N. J. Chem.* 43 (2019) 6048–6062.

[49] W.F. Zhang, Y.L. He, M.S. Zhang, Z. Yin, Q. Chen, Raman scattering study on anatase TiO₂ nanocrystals, *J. Phys. D: Appl. Phys.* 33 (2000) 912.

[50] M. Hinojosa-Reyes, R. Camposeco-Solís, R. Zanella, V. Rodríguez González, Hydrogen production by tailoring the brookite and Cu₂O ratio of sol-gel Cu-TiO₂ photocatalysts, *Chemosphere* 184 (2017) 992–1002.

[51] B. Choudhury, M. Dey, A. Choudhury, Defect generation, d-d transition, and band gap reduction in Cu-doped TiO₂ nanoparticles, *Int. Nano Lett.* 3 (2013) 25.

[52] Z. El Koura, G. Rossi, M. Calizzi, L. Amidani, L. Pasquini, A. Miotello, F. Boscherini, XANES study of vanadium and nitrogen dopants in photocatalytic TiO₂ thin films, *Phys. Chem. Chem. Phys.* 20 (2018) 221–231.

[53] Y. Zhao, Y. Zhao, R. Shi, B. Wang, G.I.N. Waterhouse, L.-Z. Wu, C.-H. Tung, T. Zhang, Tuning Oxygen Vacancies in Ultrathin TiO₂ Nanosheets to Boost Photocatalytic Nitrogen Fixation up to 700 nm, *Adv. Mater.* 31 (2019) 1806482.

[54] M. Zhu, P. Tian, R. Kurtz, T. Lunkenbein, J. Xu, R. Schlögl, I.E. Wachs, Y.-F. Han, Strong Metal-Support Interactions between Copper and Iron Oxide during the High-Temperature Water-Gas Shift Reaction, *Angew. Chem. Int. Ed.* 58 (2019) 9083–9087.

[55] X. Du, Y. Huang, X. Pan, B. Han, Y. Su, Q. Jiang, M. Li, H. Tang, G. Li, B. Qiao, Size-dependent strong metal-support interaction in TiO₂ supported Au nanocatalysts, *Nat. Commun.* 11 (2020) 5811.

[56] Q. Ma, D.B. Buchholz, R.P.H. Chang, Local structures of copper-doped ZnO films, *Phys. Rev. B* 78 (2008) 214429.

[57] Y. Okamoto, H. Gotoh, H. Aritani, T. Tanaka, S. Yoshida, Zirconia-supported copper catalysts for NO-CO reactions Surface copper species on zirconia, *Journal of the Chemical Society, Faraday Trans.* 93 (1997) 3879–3885.

[58] Y. Okamoto, T. Kubota, H. Gotoh, Y. Ohto, H. Aritani, T. Tanaka, S. Yoshida, XAFS study of zirconia-supported copper catalysts for the NO-CO reaction: Deactivation, rejuvenation and stabilization of Cu species, *Journal of the Chemical Society, Faraday Trans.* 94 (1998) 3743–3752.

[59] A. Gaur, B. Shrivastava, A Comparative Study of the Methods of Speciation Using X-ray Absorption Fine Structure, *Acta Phys. Pol. A* 121 (2012) 647–652.

[60] J. Schwan, S. Ulrich, V. Batori, H. Ehrhardt, S.R.P. Silva, Raman spectroscopy on amorphous carbon films, *J. Appl. Phys.* 80 (1996) 440–447.

[61] M.W. Smith, I. Dallmeyer, T.J. Johnson, C.S. Brauer, J.-S. McEwen, J.F. Espinal, M. Garcia-Perez, Structural analysis of char by Raman spectroscopy: improving band assignments through computational calculations from first principles, *Carbon* 100 (2016) 678–692.

[62] N. Justh, L.P. Bakos, K. Hernádi, G. Kiss, B. Réti, Z. Erdélyi, B. Parditka, I. M. Szilágyi, Photocatalytic hollow TiO₂ and ZnO nanospheres prepared by atomic layer deposition, *Sci. Rep.* 7 (2017) 4337.

[63] E. Sartoretti, C. Novara, F. Giorgis, M. Piumetti, S. Bensaid, N. Russo, D. Fino, In situ Raman analyses of the soot oxidation reaction over nanostructured ceria-based catalysts, *Sci. Rep.* 9 (2019) 3875.

[64] R.L. Frost, A. Locke, W.N. Martens, Synthesis and Raman spectroscopic characterisation of the oxalate mineral wheatleyite Na₂Cu₂+(C₂O₄)₂·2H₂O, *J. Raman Spectrosc.* 39 (2008) 901–908.

[65] K.I. Hadjivivanov, D.A. Panayotov, M.Y. Mihaylov, E.Z. Ivanova, K.K. Chakarova, S. M. Andonova, N.L. Drenchev, Power of infrared and Raman spectroscopies to characterize metal-organic frameworks and investigate their interaction with guest molecules, *Chem. Rev.* 121 (2021) 1286–1424.

[66] A.C. Ferrari, D.M. Basko, Raman spectroscopy as a versatile tool for studying the properties of graphene, *Nat. Nanotechnol.* 8 (2013) 235–246.

[67] J.-B. Wu, M.-L. Lin, X. Cong, H.-N. Liu, P.-H. Tan, Raman spectroscopy of graphene-based materials and its applications in related devices, *Chem. Soc. Rev.* 47 (2018) 1822–1873.

[68] S. Yao, K. Mudiyanselage, W. Xu, A.C. Johnston-Peck, J.C. Hanson, T. Wu, D. Stacchiola, J.A. Rodriguez, H. Zhao, K.A. Beyer, K.W. Chapman, P.J. Chupas, A. Martínez-Arias, R. Si, T.B. Bolin, W. Liu, S.D. Senanayake, Unraveling the dynamic nature of a CuO/CeO₂ Catalyst for CO oxidation in Operando: a combined study of XANES (Fluorescence) and DRIFTS, *ACS Catal.* 4 (2014) 1650–1661.

[69] P. Jiang, D. Prendergast, F. Borondics, S. Porsgaard, L. Giovanetti, E. Pach, J. Newberg, H. Bluhm, F. Besenbacher, M. Salmeron, Experimental and theoretical investigation of the electronic structure of Cu₂O and CuO thin films on Cu(110) using x-ray photoelectron and absorption spectroscopy, *J. Chem. Phys.* 138 (2013).

[70] A. Knop-Gericke, M. Hävecker, T. Schedel-Niedrig, R. Schlögl, Probing the electronic structure of an active catalyst surface under high-pressure reaction conditions: the oxidation of methanol over copper, *Catal. Lett.* 66 (2000) 215–220.

[71] A. Knop-Gericke, M. Hävecker, T. Schedel-Niedrig, R. Schlögl, High-pressure low-energy XAS: a new tool for probing reacting surfaces of heterogeneous catalysts, *Top. Catal.* 10 (2000) 187–198.

[72] A. Knop-Gericke, M. Hävecker, T. Schedel-Niedrig, R. Schlögl, Characterisation of active phases of a copper catalyst for methanol oxidation under reaction conditions: an in situ X-ray absorption spectroscopy study in the soft energy range, *Top. Catal.* 15 (2001) 27–34.

[73] D.A. Svititsitskiy, T.Y. Kardash, O.A. Stonkus, E.M. Slavinskaya, A.I. Stadnichenko, S.V. Koscheev, A.P. Chupakhin, A.I. Boronin, In situ XRD, XPS, TEM, and TPR study of highly active in CO oxidation CuO nanopowders, *J. Phys. Chem. C.* 117 (2013) 14588–14599.